optica

Water window soft x-ray source enabled by a 25 W few-cycle 2.2 μm OPCPA at 100 kHz

J. Pupeikis,* P.-A. Chevreuil, N. Bigler, L. Gallmann, C. R. Phillips, and U. Keller

Department of Physics, Institute of Quantum Electronics, ETH Zurich, Switzerland
**Corresponding author: pupeikis@phys.ethz.ch*

Received 7 October 2019; revised 15 December 2019; accepted 24 December 2019 (Doc. ID 379846); published 7 February 2020

Coherent soft x-ray (SXR) sources enable fundamental studies in the important water window spectral region. Until now, such sources have been limited to repetition rates of 1 kHz or less, which restricts count rates and signal-to-noise ratio for a variety of experiments. SXR generation at high repetition rate has remained challenging because of the missing high-power infrared laser sources to drive the high-harmonic generation (HHG) process. Here we present an optical parametric chirped pulse amplifier (OPCPA) centered at a wavelength of 2.2 μm and generating 16.5 fs pulses (2.2 oscillation cycles of the carrier wave) with 25 W of average power and a peak power exceeding 14 GW at 100 kHz pulse repetition rate. This corresponds to the highest reported peak power for high-repetition-rate long-wavelength laser systems. The output of this 2.2 μm OPCPA system was used to generate a coherent SXR radiation extending beyond 0.6 keV through HHG in a high-pressure gas cell.

https://doi.org/10.1364/OPTICA.379846

Progress in laser technology has enabled rapid development in attosecond science and led to many scientific discoveries [1,2]. Further advances in attosecond science are closely linked to high-harmonic generation (HHG) sources and therefore to state-of-the-art laser systems to drive the HHG process into new performance frontiers [3]. Specifically, there is currently great interest in scaling HHG sources to parameters beyond those available in conventional Ti:sapphire amplifier driven beamlines, in particular to higher photon energies and higher repetition rates. Photon energies extending up to 1.6 keV were generated at 20 Hz repetition rate [4]. Recently, multiple research groups have developed 0.1–1 kHz laser sources capable of producing coherent soft x-ray (SXR) radiation spanning up to the oxygen K-edge at 543 eV [5–9].

Such high-photon-energy sources are interesting for a variety of spectroscopic studies since core electrons can be accessed directly. For example, this enables direct probing of biological molecules in aqueous solutions [10] and tracking of electronic, vibrational, and rotational [11] as well as magnetization dynamics [12]. Furthermore, the high photon energies allow for the shortest attosecond pulses ever produced [13]. On the other hand, high repetition rates are especially important for applications limited by space-charge effects, such as the investigation of photoemission delays from surfaces [14,15].

The coherent SXR radiation in the above examples is generated via HHG. At a given driving laser intensity I and carrier wavelength λ, the maximum energy of the generated photons scales with $\sim I \cdot \lambda^2$ [16]. Thus, to obtain a high-energy cutoff without excessive ionization of the target, which would prevent phase matching, long-wavelength driving lasers are required. Long driving wavelengths also give rise to high phase-matching pressures, which increases the number of potential emitters [17]. On the other hand, the single-atom yield drops rapidly with wavelength, with a scaling of around $\sim \lambda^{-(5-6)}$ for a fixed energy interval [18,19]. This can lead to a significantly reduced HHG efficiency. Therefore, high-average-power laser sources with pulses providing sufficient peak power are critical. Furthermore, for experiments where few photo-ionization events per shot are required to avoid space-charge effects [20] or to enable coincidence detection [21,22], the repetition rate of the laser determines the data acquisition time.

Recently, several 10 W class laser systems operating at high repetition rates (≥100 kHz) with wavelengths above 2 μm were reported [23–27]. They represent an important advance in ultrafast laser technology. However, in the context of efficient attosecond pulse generation at high photon energies, pulse duration and peak power are of critical importance. Until now the peak power of 100 kHz laser sources operating above 2 μm was limited to 6 GW [23].

In this Letter, we present a laser system delivering pulses centered at a wavelength of 2.2 μm and with 14 GW peak power at 100 kHz repetition rate. The peak power of this laser source was sufficient to generate SXR radiation extending beyond the water window. This first demonstration of SXR generation at 100 kHz is a key enabling step for a new generation of attosecond technology where high repetition rates and high photon energies are provided simultaneously. In the following, we first present our new optical parametric chirped pulse amplifier (OPCPA) system and then show data from SXR generation experiment in helium gas, reaching photon energies up to 0.6 keV.

Figure 1 shows the conceptual layout of our OPCPA. The pumping architecture of our OPCPA is based on a Ti:sapphire laser oscillator which seeds an Innoslab amplifier system (A400,

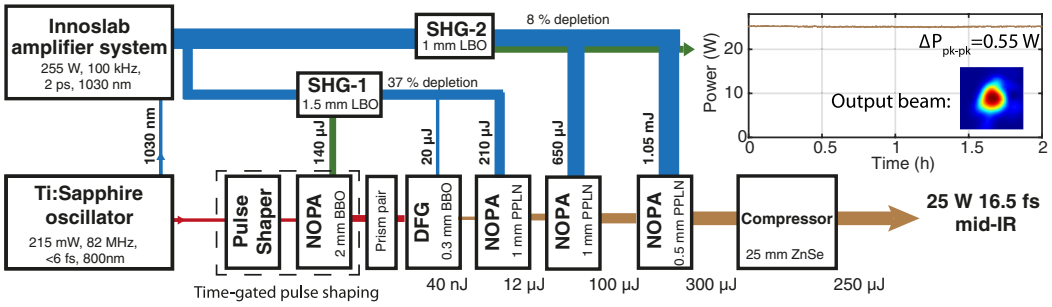

Fig. 1. Optical parametric chirped-pulse amplifier (OPCPA) layout. SHG, second harmonic generation; NOPA, noncollinear optical parametric amplifier; DFG, difference-frequency generation; BBO, beta barium borate; PPLN, periodically poled lithium niobate; LBO, lithium triborate; ZnSe, zinc selenide. The inset on the top right shows the long-term output stability of the system and beam profile after cylindrical reshaping telescopes.

Amphos GmbH). In comparison to our last result [23], we implemented significant new design steps for the OPCPA system to obtain higher performance.

First, the beam pointing of the Innoslab amplifier output is actively stabilized by using two stabilization units (TEM Messtechnik GmbH). In a first stage, the beam is stabilized on a one-dimensional spatial Fourier filter for beam cleaning. The spatially filtered beam then enters a grating compressor, where it is compressed to a duration of 2 ps (intentionally longer than the minimum supported duration of 0.95 ps). The output beam from the compressor is then spatially stabilized in a second stage to ensure a stable pump beam for the OPCPA system. The overall efficiency of this cleaning and compression unit is 61%, and the resulting total output average power is 255 W.

For the signal path of the OPCPA, we leverage a spectral-aberration-free time-gated pulse shaping technique, which is applied on the low-energy seed pulses [28]. We impose a large negative group delay dispersion (GDD) of $-2400\ \mathrm{fs}^2$ at a center wavelength of 730 nm in conjunction with a negative third-order dispersion (TOD) contribution of $-10{,}400\ \mathrm{fs}^3$. Furthermore, the Ti:sapphire spectrum is flattened via the programmable amplitude shaping capability of the pulse shaper. After shaping, the seed waveform is time-gated and amplified in a noncollinear optical parametric amplifier (NOPA) based on a 2 mm long beta barium borate (BBO) crystal in a type 1 nonlinear interaction geometry. The 515 nm NOPA pump is generated via second-harmonic generation (SHG) of a portion of the 1030 nm beam. This SHG stage (SHG-1 in Fig. 1) is deliberately configured to have a relatively low conversion efficiency to take advantage of how the SHG process reshapes the transmitted fundamental beam (explained below).

Due to the relatively high gain and short pump duration of the NOPA stage, the pulse shaper cannot impose the full dispersion needed for the OPCPA chain. Thus, the near-IR NOPA output is further stretched with a prism pair, providing additional negative GDD of $-1400\ \mathrm{fs}^2$ and TOD of $-17{,}000\ \mathrm{fs}^3$ at 730 nm. Next, the IR light is generated as an idler in a collinear 0.3 mm long BBO-based difference-frequency generation (DFG) stage. The output of the NOPA is focused into the DFG crystal to $80\ \mathrm{GW/cm}^2$ peak intensity (estimated via the measured beam size and the calculated dispersion on the pulse). It is overlapped with part of the transmitted 1030 nm beam from SHG-1, focused to $12\ \mathrm{GW/cm}^2$ peak intensity (estimated based on the measured beam size and the calculated SHG depletion from SHG-1). Because the DFG occurs between the shaped NOPA output and a fixed-phase narrowband seed, the phase defined by the pulse shaper is linearly transferred to the idler.

The generated idler pulses are amplified in three periodically poled lithium niobate (PPLN) NOPA stages with type 0 phase matching. For all of the amplification stages, we use MgO-doped PPLN samples with a high-aspect-ratio $2 \times 10.9\ \mathrm{mm}^2$ poled aperture and 29.3 µm poling period (HC Photonics Corp.). The lengths of the samples at each subsequent stage are 1, 1, and 0.5 mm. Obtaining high gain in such short PPLN samples is enabled by their large nonlinear coefficient. This leads to an octave-wide phase-matching bandwidth and minimal IR light absorption in the crystals, and it mitigates photorefractive effects due to the high-power pump pulses. Furthermore, the PPLN crystals are wrapped in indium foil and placed in water-cooled copper mounts to ensure good thermal and electrical contact.

Each amplification stage leverages the spatiotemporal flattening effects of SHG on the transmitted fundamental wave (FW). This shaping occurs because the highest-intensity parts of the input pulse are converted to the second harmonic (SH) most efficiently and thereby provide a flattening effect in both space and time on the FW. Such flattening is advantageous for mitigating back-conversion effects in subsequent frequency conversion stages.

The first PPLN NOPA stage is pumped by the transmitted FW beam from SHG-1. The second and third stages use the same principle but have a different, separately adjustable SHG crystal (SHG-2, Fig. 1). While the SH output of SHG-1 pumps the BBO NOPA, the SH output of SHG-2 is simply discarded as illustrated in Fig. 1. To preserve the flattened beam shape and also to ensure the stability of the system, the pump beams from the SHG stages are imaged with cylindrical telescopes onto the PPLN crystals at estimated peak intensities of 23, 18, and $25\ \mathrm{GW/cm}^2$. The beam flattening plays an important role in the operation of the system since it allows us to increase the useful pump energy on the crystals and helps to prevent early saturation of the amplification. Such operation conditions of the PPLN-based amplification stages permit using 100 W class pump powers with manageable thermal and photorefractive distortions on the amplified signal beams.

The last amplification stage delivers up to 30 W of output signal power with a power slope plotted in Fig. 2(a). The output beam is spatially shaped with cylindrical CaF_2 antireflection coated telescopes, spectrally filtered from any parasitic copropagating light by multiple reflections on high-reflectivity ultra-broadband mirrors based on Si/SiO_2 multilayers (Optoman), and it is finally compressed in a 25 mm thick zinc selenide (ZnSe) bulk compressor oriented at Brewster's angle. This leads to 25 W compressed IR output power available for experiments. ZnSe was chosen to compress the pulses due to its favorable GDD-to-TOD ratio.

Minimum overall TOD in the system helps to maintain a monotonic chirp of the pulses, which prevents crosstalk between the spectral components in the amplification stages.

The compressed pulses were characterized using a third-harmonic frequency-resolved optical gating technique (FROG). Figure 2(b) shows the measured and retrieved traces. Figures 2(c) and 2(d) show the retrieved pulse duration and spectrum compared with an independently measured spectrum. The retrieved spectral phase is virtually flat over the full spectral range. The retrieved pulse shape yields a transform-limited 16.5 fs FWHM duration. The peak power of the pulses was calculated to be 14.2 GW, which corresponds to the highest peak power reported for high-repetition-rate systems. The central wavelength of the output spectrum was calculated to be 2.2 μm; thus the pulse envelope contains only 2.2 oscillation cycles of the carrier wave at FWHM.

Compared to our previous OPCPA result [23], this system operates in a regime of opposite GDD sign, which allowed us to decrease the overall TOD. The system also contains one amplification stage less while providing a higher conversion efficiency. In particular, the quantum conversion efficiency in the final stage is as high as 41%. The spatiotemporal flattening of the pump beam for the PPLN-based NOPA stages allowed us to maximize energy extraction from the pump while keeping a broadband amplification thanks to the improved pump pulse temporal shape.

For HHG experiments, the output beam of our OPCPA is routed via a periscope system to another laboratory more than 15 m away from the output of the system. The beam is guided by high-reflectivity Si/SiO_2 mirrors (Optoman), and its pointing is stabilized on another optical table using a stabilization unit (TEM Messtechnik GmbH). The beam path, including the OPCPA system itself, is immersed in nitrogen gas to minimize water vapor absorption.

For ionizing helium, the beam was tightly focused with a 75 mm long focal length plano-convex CaF_2 lens. Using a ray-tracing software (Zemax) and assuming a diffraction-limited beam input beam, we estimate a beam waist of 40 μm at the focus. Spatial and chromatic aberrations were included in the calculation. In the experiment, the focus position was optimized for the highest total flux. The tight focusing leads to a strong Gouy-phase sweep through the interaction length. On top of that, the refractive index of helium at IR and SXR wavelengths is close to unity. Thus, a high gas density is necessary to compensate for the Gouy phase and ionization of helium in order to achieve phase-matching conditions between the IR and the SXR radiation [17]. From our calculations, we have found that a target pressure of 20–50 bar is necessary to phase match 2.2 μm driven HHG in helium. Because of this reason, we have used a stainless-steel needle with 1 mm inner diameter and 100 μm thick walls transversally drilled by the laser itself.

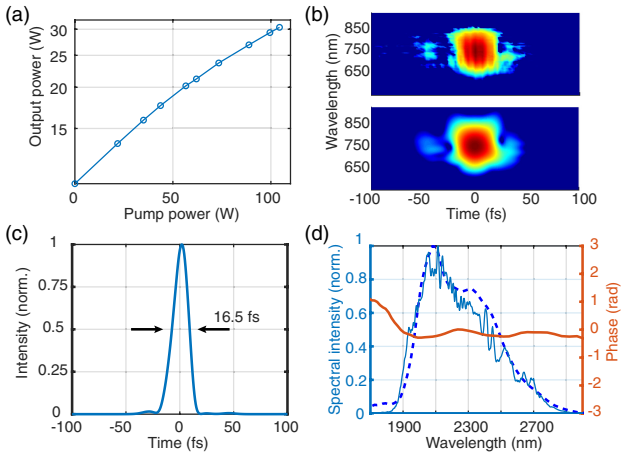

Fig. 2. (a) Power slope of the last amplification stage. (b) Measured (top) and reconstructed (bottom) FROG traces with an error of 1.1% using a grid of 128 × 128 points. The FROG signal was generated on the surface of a CaF_2 plate. (c) The retrieved pulse shape of the amplifier output. (d) Blue line, measured spectrum; blue-dashed line, retrieved spectrum; orange line, retrieved phase.

To ensure that a high vacuum state can be maintained after the HHG despite the required gas pressure, a differential pumping scheme was implemented (see Fig. 3). Our HHG module uses two differential pumping stages. The first stage (red-dashed path) is pumped by a high-gas-load pump (A100L, Pfeiffer), while the second stage (yellow-dashed path) is already supported by a turbomolecular pump (HP300, Pfeiffer). The pressure in the stages was defined by the hole size in the needle. With two mechanically drilled 60 μm diameter holes, we could supply more than 70 bar target gas pressure. At such conditions, the pressure is 7 mbar in the first and $1.5 \cdot 10^{-2}$ mbar in the second stage. The input gas pressure was measured directly on the delivery line and is expected to be the same at the interaction point since the gas undergoes no free expansion before interaction.

The HHG module output is directly connected to a larger vacuum chamber with a residual gas pressure below 10^{-6} mbar for HHG characterization with a CCD-based (Andor Newton 940) flat-field spectrometer (251 MX, McPherson). The spectrometer entrance slit was set to have 1 mm width for all presented measurements, and it was positioned 90 cm away from the target gas cell. The spectra were measured after blocking the residual pump light with a 100 nm thick aluminum filter. The spectrometer was calibrated on the observed absorption edges and by the position of harmonics where they are resolved. The carbon K-edge is visible in all measurements and originates from contamination in the spectrometer. The measured spectra were corrected for the CCD response, the grating reflectivity, and the filter transmission.

Figure 4 shows our results with helium, demonstrating HHG spanning the water window spectral region. The spectrum is recorded to extend up to 620 eV at 45 bar target pressure. From the cutoff, the achieved peak intensity was estimated to be 420 TW/cm^2 with 220 μJ input pulse energy. At this pressure, the absorption length for 400 eV photons in helium gas is 1.2 mm. Thus, reabsorption in the gas does not significantly reduce the SXR flux. From spatiotemporal phase-matching calculations based on Perelomov-Popov-Terent'ev ionization rates [29], we find that the maximum attainable coherence length of the HHG is below 1 mm

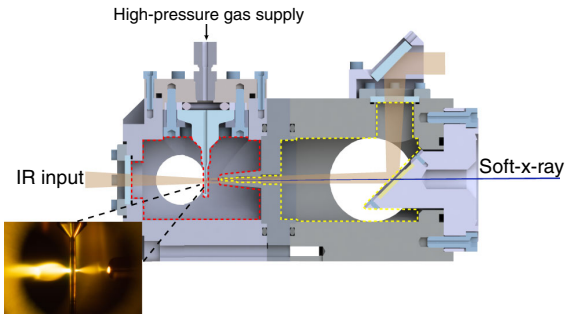

Fig. 3. HHG with differential gas pumping. Red- and yellow-dashed paths mark the first and second differential pumping stages, respectively. Inset: photo taken during the HHG process.

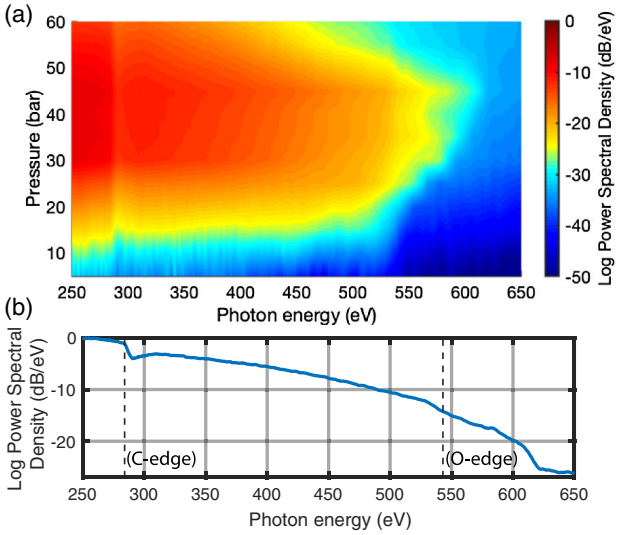

Fig. 4. Measured HHG spectrum (a) from helium target gas as a function of the target pressure, and (b) at 45 bar helium gas pressure. Integration time for each measurement was set to 60 s.

for our parameters, and the absorption-limited HHG conditions are not met [30]. The absolute flux of the HHG was not measured due to the lack of a suitable calibrated measurement device, but from the CCD counts the lower bound of the flux entering the spectrometer is estimated to be 32 pW between 250 and 620 eV. This estimate does not include possible beam clipping on the entrance slit or the differential pumping module, and thus the absolute conversion efficiency cannot be estimated.

We have demonstrated a 100 kHz 2.2 μm laser source delivering pulses with peak power over 14 GW and average power of 25 W. To our knowledge, this corresponds to the world record output parameters for high-repetition-rate systems with wavelengths above 2 μm. The two-cycle pulses from the OPCPA system were used to generate SXR spectrum spanning the complete water window up to 0.6 keV. This proof-of-principle demonstration paves the way for high-repetition-rate experiments in the water window range. This laser source will enable a new generation of attosecond studies, where high repetition rates and high photon energies are combined to explore new regimes with space-charge-free ultrafast photoemission and coincidence detection techniques.

Funding. Swiss National Science Foundation (200020_172644, 206021_164034/1).

Acknowledgment. We thank Marcel Baer and Andreas Stuker with their teams for support in preparing custom mechanical components and vacuum chambers. We also thank Benjamin Willenberg, Fabian Brunner, and Stefan Hrisafov for their advice and support in the lab.

Disclosures. The authors declare no conflicts of interest.

REFERENCES

1. F. Krausz and M. Ivanov, Rev. Mod. Phys. **81**, 163 (2009).
2. L. Gallmann, C. Cirelli, and U. Keller, Annu. Rev. Phys. Chem. **63**, 447 (2012).
3. X. Ren, J. Li, Y. Yin, K. Zhao, A. Chew, Y. Wang, S. Hu, Y. Cheng, E. Cunningham, Y. Wu, M. Chini, and Z. Chang, J. Opt. **20**, 023001 (2018).
4. T. Popmintchev, M.-C. Chen, D. Popmintchev, P. Arpin, S. Brown, S. Alisauskas, G. Andriukaitis, T. Balciunas, O. D. Mucke, A. Pugzlys, A. Baltuska, B. Shim, S. E. Schrauth, A. Gaeta, C. Hernandez-Garcia, L. Plaja, A. Becker, A. Jaron-Becker, M. M. Murnane, and H. C. Kapteyn, Science **336**, 1287 (2012).
5. C. Schmidt, Y. Pertot, T. Balciunas, K. Zinchenko, M. Matthews, H. J. Wörner, and J.-P. Wolf, Opt. Express **26**, 11834 (2018).
6. S. M. Teichmann, F. Silva, S. L. Cousin, M. Hemmer, and J. Biegert, Nat. Commun. **7**, 11493 (2016).
7. D. Popmintchev, B. R. Galloway, M. Chen, F. Dollar, C. A. Mancuso, A. Hankla, L. Miaja-Avila, G. O'Neil, J. M. Shaw, G. Fan, S. Ališauskas, G. Andriukaitis, T. Balčiunas, O. D. Mücke, A. Pugzlys, A. Baltuška, H. C. Kapteyn, T. Popmintchev, and M. M. Murnane, Phys. Rev. Lett. **120**, 093002 (2018).
8. V. Cardin, B. E. Schimdt, N. Thiré, S. Beaulieu, V. Wanie, M. Negro, C. Vozzi, V. Tosa, and F. Légaré, J. Phys. B **51**, 174004 (2018).
9. A. S. Johnson, D. R. Austin, D. A. Wood, C. Brahms, A. Gregory, K. B. Holzner, S. Jarosch, E. W. Larsen, S. Parker, C. S. Strüber, P. Ye, J. W. G. Tisch, and J. P. Marangos, Sci. Adv. **4**, eaar3761 (2018).
10. I. Jordan, M. Huppert, M. A. Brown, J. A. van Bokhoven, and H. J. Wörner, Rev. Sci. Instrum. **86**, 123905 (2015).
11. N. Saito, H. Sannohe, N. Ishii, T. Kanai, N. Kosugi, Y. Wu, A. Chew, S. Han, Z. Chang, and J. Itatani, Optica **6**, 1542 (2019).
12. B. Vodungbo, J. Gautier, G. Lambert, A. B. Sardinha, M. Lozano, S. Sebban, M. Ducousso, W. Boutu, K. Li, B. Tudu, M. Tortarolo, R. Hawaldar, R. Delaunay, V. López-Flores, J. Arabski, C. Boeglin, H. Merdji, P. Zeitoun, and J. Lüning, Nat. Commun. **3**, 999 (2012).
13. T. Gaumnitz, A. Jain, Y. Pertot, M. Huppert, I. Jordan, F. Ardana-Lamas, and H. J. Wörner, Opt. Express **25**, 27506 (2017).
14. A. L. Cavalieri, N. Müller, T. Uphues, V. S. Yakovlev, A. Baltuška, B. Horvath, B. Schmidt, L. Blümel, R. Holzwarth, S. Hendel, M. Drescher, U. Kleineberg, P. M. Echenique, R. Kienberger, F. Krausz, and U. Heinzmann, Nature **449**, 1029 (2007).
15. L. Kasmi, M. Lucchini, L. Castiglioni, P. Kliuiev, J. Osterwalder, M. Hengsberger, L. Gallmann, P. Krüger, and U. Keller, Optica **4**, 1492 (2017).
16. J. L. Krause, K. J. Schafer, and K. C. Kulander, Phys. Rev. Lett. **68**, 3535 (1992).
17. T. Popmintchev, M.-C. Chen, A. Bahabad, M. Gerrity, P. Sidorenko, O. Cohen, I. P. Christov, M. M. Murnane, and H. C. Kapteyn, Proc. Natl. Acad. Sci. USA **106**, 10516 (2009).
18. J. Tate, T. Auguste, H. G. Muller, P. Salières, P. Agostini, and L. F. DiMauro, Phys. Rev. Lett. **98**, 013901 (2007).
19. A. D. Shiner, C. Trallero-Herrero, N. Kajumba, H.-C. Bandulet, D. Comtois, F. Légaré, M. Giguère, J.-C. Kieffer, P. B. Corkum, and D. M. Villeneuve, Phys. Rev. Lett. **103**, 073902 (2009).
20. S. Passlack, S. Mathias, O. Andreyev, D. Mittnacht, M. Aeschlimann, and M. Bauer, J. Appl. Phys. **100**, 024912 (2006).
21. J. Ullrich, R. Moshammer, A. Dorn, R. Dorner, L. P. H. Schmidt, and H. Schmidt-Bocking, Rep. Prog. Phys. **66**, 1463 (2003).
22. M. Sabbar, S. Heuser, R. Boge, M. Lucchini, L. Gallmann, C. Cirelli, and U. Keller, Rev. Sci. Instrum. **85**, 103113 (2014).
23. N. Bigler, J. Pupeikis, S. Hrisafov, L. Gallmann, C. R. Phillips, and U. Keller, Opt. Express **26**, 26750 (2018).
24. N. Thiré, R. Maksimenka, B. Kiss, C. Ferchaud, G. Gitzinger, T. Pinoteau, H. Jousselin, S. Jarosch, P. Bizouard, V. Di Pietro, E. Cormier, K. Osvay, and N. Forget, Opt. Express **26**, 26907 (2018).
25. M. Neuhaus, H. Fuest, M. Seeger, J. Schötz, M. Trubetskov, P. Russbueldt, H. D. Hoffmann, E. Riedle, Z. Major, V. Pervak, M. F. Kling, and P. Wnuk, Opt. Express **26**, 16074 (2018).
26. U. Elu, M. Baudisch, H. Pires, F. Tani, M. H. Frosz, F. Köttig, A. Ermolov, P. St. J. Russell, and J. Biegert, Optica **4**, 1024 (2017).
27. M. Mero, Z. Heiner, V. Petrov, H. Rottke, F. Branchi, G. M. Thomas, and M. J. J. Vrakking, Opt. Lett. **43**, 5246 (2018).
28. J. Pupeikis, N. Bigler, S. Hrisafov, C. R. Phillips, and U. Keller, Opt. Express **27**, 175 (2019).
29. Y. H. Lai, J. Xu, U. B. Szafruga, B. K. Talbert, X. Gong, K. Zhang, H. Fuest, M. F. Kling, C. I. Blaga, P. Agostini, and L. F. DiMauro, Phys. Rev. A **96**, 063417 (2017).
30. E. Constant, D. Garzella, P. Breger, E. Mével, C. Dorrer, C. Le Blanc, F. Salin, and P. Agostini, Phys. Rev. Lett. **82**, 1668 (1999).